



Multi-microenvironment synergistically promoting CO₂ electroreduction activity on porous Cu nanosheets

Dan Wang^a, Jianing Gui^a, Binbin Pan^b, Mengxuan Li^c, Yun Kuang^c, Chenchen Zhang^a, Junjun Mao^a, Yang Lou^a, Chengsi Pan^a, Fengwang Li^d, Yanguang Li^b, Yuhang Wang^{b,*}, Yongfa Zhu^{e,*}, Ying Zhang^{a,*}

^a Key Laboratory of Synthetic and Biological Colloids Ministry of Education, School of Chemical and Material Engineering, Jiangnan University, Wuxi, Jiangsu 214122, China

^b Institute of Functional Nano & Soft Materials (FUNSOM), Jiangsu Key Laboratory for Carbon-Based Functional Materials and Devices, Soochow University, Suzhou 215123, China

^c State Key Laboratory of Chemical Resource Engineering, Beijing Advanced Innovation Center for Soft Matter Science and Engineering, College of Chemistry, Beijing University of Chemical Technology, Beijing 100029, China

^d School of Chemical and Biomolecular Engineering, University of Sydney, NSW 2006, Australia

^e Department of Chemistry, Tsinghua University, Beijing 100084, China



ARTICLE INFO

Keywords:

Cu nanosheets
Porous structure
Microenvironment
CO₂ accessibility
Local pH

ABSTRACT

Adjusting the microstructure of Cu/Cu-based catalysts is a typical approach to tuning ECO₂RR performance, while the effects among microstructure and the induced multi-microenvironment variations for ECO₂RR performance are still not very clear. Herein, a controllable way to introduce nanoporous structures on Cu nanosheets (Cu NSS) to modulate the surface and reaction microenvironment for synergistically improving ECO₂RR activity is proposed. Larger nanopores uniformly distributed on Cu NSS can firstly improve the surface microenvironment by enhancing hydrophobic and CO₂-philic properties, which promote the accessibility of CO₂ and help to suppress hydrogen evolution reaction. Furthermore, this microstructure also can adjust the reaction microenvironment by attracting and aggregating OH⁻ anions to enhance the local pH, which helps promote the C-C coupling for C₂H₄ formation. These findings suggest that modulating microstructure can regulate multi-microenvironment including improving the accessibility of CO₂ and constructing a higher local pH near the active sites to synergistically promote ECO₂RR activity.

1. Introduction

Among various catalytic materials for electrochemical CO₂ reduction reaction (ECO₂RR), Cu metal and Cu-based catalysts were found to produce valuable multi-carbon (C₂₊) products in aqueous solutions due to their negative adsorption energy toward *CO and positive adsorption energy for *H [1–5]. The selective production of C₂₊ products remains challenging because of the competing hydrogen evolution reaction (HER) and the sluggish kinetics of the C-C coupling step, a key step to generating C₂₊ products [6,7]. Most previous works have been focused on designing and tuning Cu/Cu-based catalysts with high selectivity toward CO₂ transformation, especially for C₂₊ products. Controlling composition and morphology [8–11], introducing grain boundaries [12, 13], and defect engineering [14,15] have been widely explored to

increase the number of active sites and improve the intrinsic catalytic activities of Cu/Cu-based catalysts for the desired ECO₂RR products. Although multiple microstructure regulation strategies have been reported to modulate the ECO₂RR performance on Cu/Cu-based catalysts, the relationship between microstructure and microenvironment has not been sufficiently studied, especially the microstructure-induced multi-microenvironment for synergistic improving the ECO₂RR activity.

For aqueous ECO₂RR, CO₂ and H₂O are the requirement reactants, while the competitive HER from H₂O strongly limits the ECO₂RR selectivity. Optimizing the ratio of CO₂ and H₂O on the catalytic layer is necessary for forming stable solid-liquid-gas triple-phase junctions to enhance the accessibility of CO₂ and suppress HER, facilitating faster CO₂ conversion [16,17]. Adding hydrophobic polytetrafluoroethylene (PTFE) nanoparticles in the catalytic layer is usually used to optimize the

* Corresponding authors.

E-mail addresses: yhwang1988@suda.edu.cn (Y. Wang), zhuuyf@mail.tsinghua.edu.cn (Y. Zhu), ying.zhang@jiangnan.edu.cn (Y. Zhang).

local $\text{CO}_2/\text{H}_2\text{O}$ ratio [18,19], while the non-conducting PTFE nanoparticles in the catalytic layer will cover parts of active sites of catalysts and impact the electrical conductivity of electrodes. Therefore, it is necessary to increase the self-hydrophobicity of catalysts, and at the same time avoid the adverse impact on blocking active sites when adding hydrophobic additives. Inspired by the porous structure of the gas diffusion electrode (GDE) which makes it has better hydrophobic and gas-permeable properties, therefore, we introduce this structure to regulate the surface microenvironment for improving the self-hydrophobicity of Cu NSs to promote CO_2 transportation.

Moreover, apart from improving the local $\text{CO}_2/\text{H}_2\text{O}$ ratio, the porous structure can also be used to construct a higher local pH near the active sites, which is an important reaction microenvironment promoting the C-C coupling process [20,21]. For example, Sargent et al. reported that more concentrated alkaline condition helps to provide high selectivity for C_{2+} products and reduce overpotentials for the ECO₂RR [22,23]. Zhang et al. reported that the adsorption and enrichment of OH^- on nanodefected Cu NSs can promote the C-C coupling for C_2H_4 formation [14]. Xie et al. reported that the energy barrier of the rate-limiting COCO* hydrogenation step, the critical intermediates in the pathway of CO_2 reduction to C_{2+} products, could be decreased under the increased local pH level [24].

Herein, lateral micron-sized Cu NSs with different nanopore sizes were designed in this work as the model catalysts to explore the synergistic effects of microstructure-induced surface and reaction microenvironments on ECO₂RR performance. Experimental results reveal that porous structures on Cu NSs help to attract and aggregate OH^- anions from the bulk electrolyte to enhance the local pH, promoting C-C coupling and resulting in higher C_2H_4 selectivity formation. Furthermore, larger nanopores uniformly distributed on Cu NSs enhance the CO_2 -philic property and weaken their hydrophilicity, which can promote the accessibility of CO_2 and thereby result in facilitating faster CO_2 conversion. Therefore, introducing nanopores to modulate the surface microstructure is capable of inducing surface and reaction microenvironments variations including enhancing the accessibility of CO_2 and constructing a higher local pH, which synergistically improve the ECO₂RR performance. Investigating the microstructure-induced multiple microenvironments for regulating ECO₂RR activity is useful for understanding the intrinsic correlations between the surface and reaction microenvironments with the catalytic performance of ECO₂RR, which offers insight into promoting other ECO₂RR catalysts.

2. Experimental section

2.1. Synthesis of precursor CuO NSs

Firstly, 6 mL of n-butylamine was dissolved into 54 mL of distilled water, and 2.4 g of $\text{Cu}(\text{CH}_3\text{COO})_2 \cdot \text{H}_2\text{O}$ was dissolved into 180 mL of distilled water. Then the n-butylamine aqueous solution was dropwise added to the copper acetate aqueous solution via peristaltic pumps under intensely stirring and keeping intensely stirring for one hour. The obtained blue precipitate mixture was placed into an 80 °C water bath under intensely stirring for 4 h. The brown precipitation was washed with distilled water and ethanol for several times and finally dried at 60 °C for 6 h. The theoretical and practical yield of CuO is 960 and 952.6 mg, respectively. The production rate of CuO is as high as 99.23 %. Finally, the prepared CuO was calcined at 200/300/400/600/800 °C for 2 h with a heating speed of 1 °C per minute in the muffle furnace. The obtained precursor CuO NSs were used to prepare Cu NSs during the electroreduction process.

2.2. Electrocatalytic CO_2 reduction measurements

Cyclic voltammetry (CV) measurements were carried out in a 0.5 M KHCO_3 aqueous solution saturated with CO_2 in a conventional three-electrode cell. The three-electrode cell comprises a Pt foil counter

electrode, an Ag/AgCl (3 M KCl) reference electrode, and a glassy carbon (0.0707 cm²) as the working electrode. 10 mg of precursor CuO NSs and 50 μL nafton (5 %) were dispersed into 950 μL methanol under sonication for 1 h to form a homogeneous CuO ink. 7 μL catalyst ink was drop-casted onto glassy carbon and dried under an infrared lamp. For the OH^- adsorption test, the catalysts were uniformly dispersed on a glassy-carbon electrode and activated in a CO_2 -saturated 0.1 M KHCO_3 electrolyte. Then the electrode was transferred to 0.1 M KOH electrolyte with the CV method at a scan rate interval of 1 mV s⁻¹. The electrolysis process was performed in a flow cell configuration. The flow cell configuration was made up of a gas-diffusion layer (H14C9, Freudenberg) used as the cathode electrode, a Pt mesh (1.2 cm × 1.5 cm, 0.5 mm thickness) used as the anode electrode. The cathode and anode cells were separated by an anion exchange membrane (X37-50 Grade T, Dioxide Materials). These three components were positioned and clamped together using polytetrafluoroethylene (PTFE) spacers. The Ag/AgCl (3.5 M KCl) was used as the reference electrode. The area of the working electrode is 1.5 × 1.5 cm², and the catalyst loading of the working electrode is about 0.25 mg cm⁻². All potential measurements were converted to the RHE based on the following formula: $E (\text{V vs. RHE}) = E (\text{V vs. Ag/AgCl}) + 0.0591 \text{ V} \times \text{pH} + 0.205 \text{ V}$. The potentials (V vs. RHE) were estimated using the pH value of the electrolyte exiting the flow cell configuration. The pH value of the 3 M KOH is about 14. The applied potentials in $E (\text{V vs. Ag/AgCl})$ and $E (\text{V vs. RHE})$ before and after iR correction forms are listed in Table S1. The CO_2 flow was controlled at 25 sccm by an ALICAT mass flow controller. The electrolyte was circulated through the electrochemical cell by a peristaltic pump (BQ 80S, Lead Fluid) with a flow rate of 11 mL min⁻¹. All the electrolysis measurements were powered by an electrochemical workstation (CS310H, Wuhan Corrttest Instruments Corp., Ltp) at room temperature and pressure. The gaseous products were analyzed by Gas Chromatograph. The liquid product was quantitatively analyzed by 1 H Nuclear Magnetic Resonance Spectroscopy with 500 μL electrolyte mixed with 200 μL D_2O and 100 μL DMSO with a certain concentration used as an internal standard.

2.3. In situ Raman spectroscopy

Smart Raman confocal-micro-Raman module equipped with a 532 nm excitation laser was used for Raman measurement with a × 50 objective lens under the backscattering geometry. The module was developed by the Institute of Semiconductors Chinese Academy of Sciences, which is coupled with a Horiba iHR550 spectrometer and a charge-coupled device (CCD) detector. Before the experiments, calibration was carried out based on the peak at 520.7 cm⁻¹ of a silicon wafer standard. Raman spectra were acquired in a custom-built Raman flow cell. During the in-situ experiment, a peristaltic pump (BQ 80S, Lead Fluid) was used to control the electrolyte flow rate at 1 mL min⁻¹, while the flow rate of CO_2 was kept at 20 sccm with a mass flow controller (Alicat MQ). The gas diffuser layers loaded with CuO-0-Cu and CuO-300-Cu NSs were taken as the working electrodes. Pt wire and Ag/AgCl were used as the counter electrode and reference electrode, respectively. The cathode and anode cells were separated by an anion exchange membrane (X37-50 Grade T, Dioxide Materials). To detect the calibration curve for local pH utilizing the HCO_3^- and CO_3^{2-} peak area ratio. The Raman spectra were collected in a Raman flow cell electrolyzer, where standard solutions (containing different ratios of KHCO_3 and K_2CO_3 , totaling 1 M electrolyte concentration) with different pH values flowed over the gas diffuser layer and Ar flowed at the back of the GDE. The solution flow rate was controlled at 1 mL min⁻¹ with a peristaltic pump and the gas flow rate was controlled at 20 sccm with a mass flow controller.

3. Results and discussion

3.1. Modulating the surface microstructure and ECO₂RR performance

Porous Cu NSs were derived by electroreduction of the porous CuO NSs. Firstly, the gram-scale productivity CuO NSs were synthesized via a facile precipitation and heat treatment process as illustrated in Fig. S1a and b. Then the prepared CuO NSs were calcined from 200 to 800 °C (referred the thermogravimetric curve as shown in Fig. S2) for 2 h to regulate their microstructure. The morphologies of CuO NSs before and after calcination at different temperatures are shown in Fig. S3. The prepared CuO exhibits the lateral micron-sized nanosheet morphology with an average length and width of about 1 μm and 200 nm, respectively. The high-resolution transmission electron microscopy (HRTEM) images in Figs. S3 and 4 exhibit that nanopores of different sizes were formed on CuO NSs after calcination at different temperatures (denoted as CuO-x, x is the calcination temperature). It is obvious that the surface roughness of CuO NSs increases after thermal oxidation, and nanopores

are uniformly distributed on CuO-300 NSs, therefore, CuO-300 is taken as an example to investigate the structure transformation from oxide copper to metal copper. The surface area and pore size of CuO-300 NSs were measured by N₂ adsorption-desorption isothermal as shown in Fig. S5. The porous structures formed due to losing the crystal water during the calcination process by analyzing the infrared spectra of precursor CuO and CuO-300 NSs shown in Fig. S6 and the thermogravimetric curve as shown in Fig. S2. Porous Cu NSs were obtained via in-situ electroreduction of the prepared porous CuO NSs. The electro-reduction potential used is more negative than -0.4 V vs. RHE (all potentials hereafter are given with respect to RHE) according to the reduction potential of Cu²⁺ to Cu⁺(~0.2 V) and Cu⁺ to Cu⁰(~-0.3 V) [25] shown in the cyclic voltammetry (CV) profile of CuO (Fig. S7). In-situ Raman spectra in Fig. S8 exhibit the gradual disappearance of CuO Raman peaks[26,27] after 60 s electroreduction, indicating the structural transformation from CuO NSs to Cu NSs. The crystal structure and surface valence state of the precursor CuO, porous CuO-300 and their corresponding electroreduced Cu NSs were characterized by the

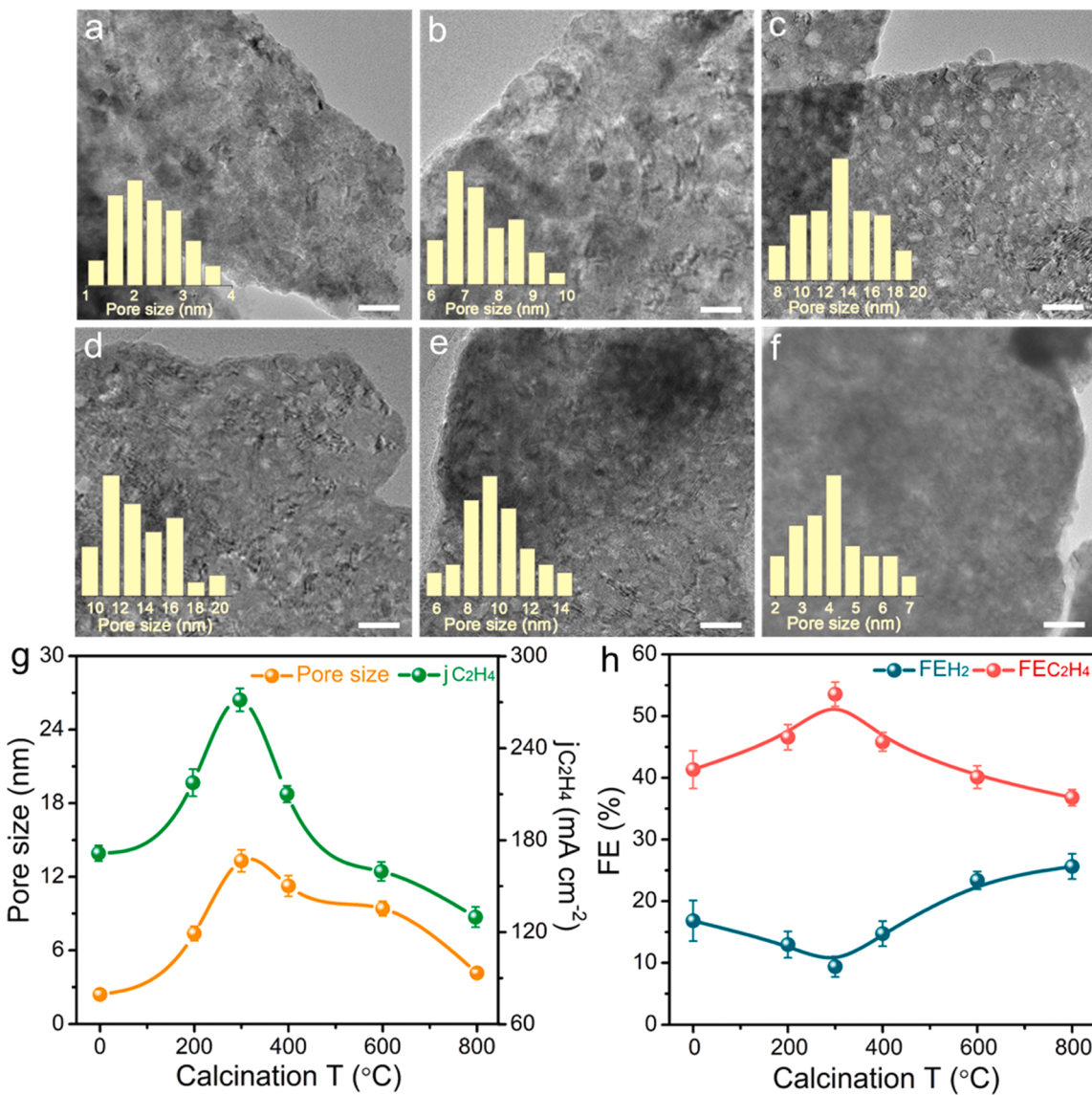


Fig. 1. Microstructure and ECO₂RR performance. TEM images of Cu NSs derived from CuO NSs before and after calcination at different temperatures: (a) CuO-0-Cu, (b) CuO-200-Cu, (c) CuO-300-Cu, (d) CuO-400-Cu, (e) CuO-600-Cu and (f) CuO-800-Cu. Histograms insert in (a-f) show the nanopore size distributions of the corresponding Cu NSs. The scale bar of (a-f) is 50 nm. (g) Average nanopore sizes (in the orange line) and partial current densities for C₂H₄ (in the green line) of Cu NSs derived from CuO NSs before and after calcination at different temperatures. (h) FEs for C₂H₄ and H₂ on Cu NSs derived from CuO NSs before and after calcination at different temperatures.

X-ray diffraction technique and X-ray photoelectron spectroscopy in Fig. S9.

Fig. 1a-f show the morphology of the in-situ electroreduced Cu from CuO NSs before and after calcination at different temperatures (denoted as CuO-x-Cu, x is the calcination temperature). CuO-x-Cu NSs show a rough surface having nanopores of different sizes, which are similar to that of CuO-x NSs (Fig. S4), indicating that the microstructure of precursor CuO-x NSs remains after the electroreduction process. Additionally, atomic force microscopic results also verify the existence of porous structures and show that the thickness of porous CuO and electro-reduced Cu NSs are measured to be about 1 nm as shown in Fig. S10. The histograms insert in Fig. 1a-f show the nanopore size distributions of CuO-x-Cu NSs. The average nanopore sizes present an approximate volcano-type trend with the increase of calcination temperatures shown in the orange line in Fig. 1g. CuO-x-Cu NSs with different nanopore sizes were used as the model catalysts for exploring the influence of surface microstructure on ECO₂RR. The ECO₂RR was conducted with a three-electrode flow cell electrolyzer using GDE as the working electrode in a 3 M KOH electrolyte solution, the Faradaic efficiencies (FEs) for C₂H₄ and H₂ are shown in Fig. 1h. The ECO₂RR selectivity to C₂H₄ on CuO-x-Cu NSs also presents an approximate volcano-type trend, which is consistent with the variation trend of nanopore sizes on CuO-x-Cu NSs. While the FEs of the competing HER present an opposite trend with the variation of nanopore sizes on CuO-x-Cu NSs. Combining with the morphology of CuO-x-Cu NSs and the ECO₂RR results, it can be seen that the largest FE for C₂H₄ can be obtained on the porous CuO-300-Cu NSs with a rough surface and the largest nanopore size, while the FEs for C₂H₄ decrease and H₂ increase on CuO-0-Cu and CuO-800-Cu NSs with relatively smooth surfaces and smaller nanopore sizes. Furthermore, the partial current densities for C₂H₄ vary along with the variation trend of nanopore sizes on CuO-x-Cu NSs, as shown in the green line in Fig. 1g, the highest partial current density for C₂H₄ was also obtained on porous CuO-300-Cu NSs with the largest nanopore size.

3.2. Insights into synergistic effects of microstructure-induced multi-microenvironment

To explore the reason for the discrepant ECO₂RR performance on CuO-x-Cu NSs with different surface microstructures, the hydrophobicity and CO₂-philicity of CuO-x-Cu NSs were investigated. As shown in Fig. 2a, the water contact angles and CO₂ contact angles of CuO-x-Cu NSs vary along with the nanopore sizes of CuO-x-Cu NSs (caused by the calcination temperature on precursor CuO NSs). CuO-0-Cu NSs with flat surfaces distributed with few small nanopores (average ~ 2 nm)

show a small water contact angle of 99° and a large CO₂ contact angle of 117°, indicating relatively hydrophilic and CO₂-phobic properties. Similar to CuO-0-Cu NSs, CuO-800-Cu NSs with similar porous structures (average nanopore size is ~ 4 nm) also show hydrophilic and CO₂-phobic properties with a smaller water contact angle of 79° and a larger CO₂ contact angle of 130°. Differ from the above samples, CuO-300-Cu NSs with rough surfaces distributed with uniform nanopores (average ~ 13 nm) show the largest water contact angle of 129° and the smallest CO₂ contact angle of 104°, revealing the hydrophobicity and CO₂-philicity of porous CuO-300-Cu NSs. Schematic illustrations of the surface microenvironment near Cu NSs without/with obvious porous structures are shown in Fig. 2b and c to help understand the discrepant ECO₂RR performance on Cu NSs with different surface microstructures. Cu NSs load on one side of the microporous layer of GDE, while CO₂ is introduced from the other side. ECO₂RR takes place at the solid-liquid-gas triple-phase junctions where the Cu NSs contact with both the electrolyte and CO₂. As shown in Fig. 2b, hydrophilic Cu NSs exhibiting smooth surfaces without obvious porous structures are easily covered by the electrolyte, inducing limited CO₂ diffusion and adsorption toward the catalytic layer and building few triple-phase junctions for ECO₂RR, resulting in the competitive HER from H₂O strongly limits the ECO₂RR selectivity (experimentally increasing the FE for H₂ as shown in Fig. 1h). Differ from Cu NSs without obvious porous structures, hydrophobic porous Cu NSs only partially in contact with the electrolyte, inducing enhanced CO₂ diffusion and adsorption toward the catalytic layer (Fig. 2c), which promotes the accessibility of CO₂ to the active sites, thus creating abundant triple-phase junctions for ECO₂RR, facilitating faster CO₂ conversion (experimentally increasing the partial current density for C₂H₄ as shown in Fig. 1g). Therefore, the enhanced ECO₂RR activity on porous Cu NSs with rough surfaces and larger nanopore size reveals the key role of microstructure in modulating the surface microenvironment for improving the ECO₂RR performance.

Apart from regulating the surface microenvironment, the porous structure can also be used to adjust the reaction microenvironment, for example constructing a higher local pH near active sites for promoting C-C coupling to increase C₂₊ production [28,29]. To verify this inference, the OH⁻ electrochemical adsorption (OH_{ads}) and local pH on the in-situ electroreduced Cu NSs were determined by CV and in-situ Raman spectroscopy. The CV curves in Fig. 3a show that the porous CuO-300-Cu NSs present pronounced (100), (110), and (111) OH_{ads} peaks [30,31], while CuO-0-Cu NSs only present a weak (111) OH_{ads} peak. The OH_{ads} results suggest that the nanoporous structures on CuO-300-Cu NSs tend to attract and aggregate OH⁻ anions on their surfaces, which would react with the introduced CO₂ to form dissolved HCO₃⁻ or CO₃²⁻ in the

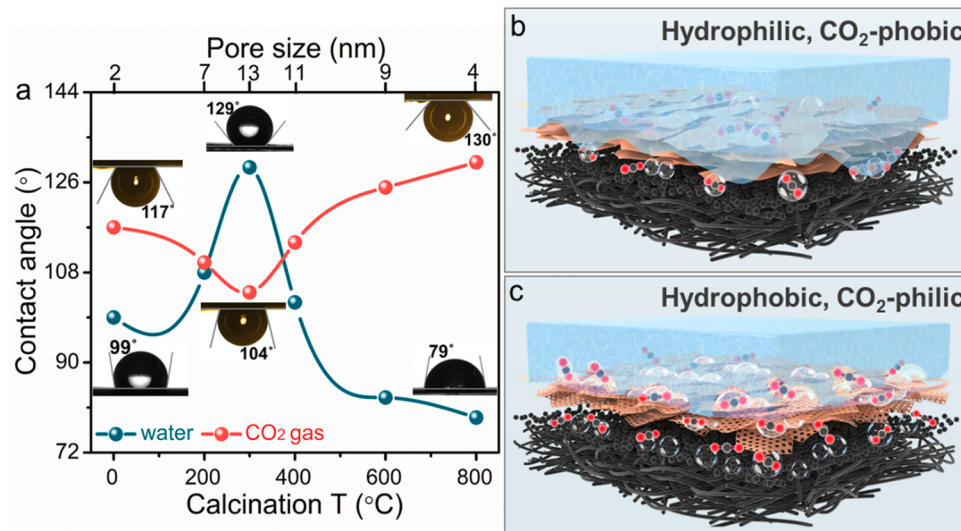
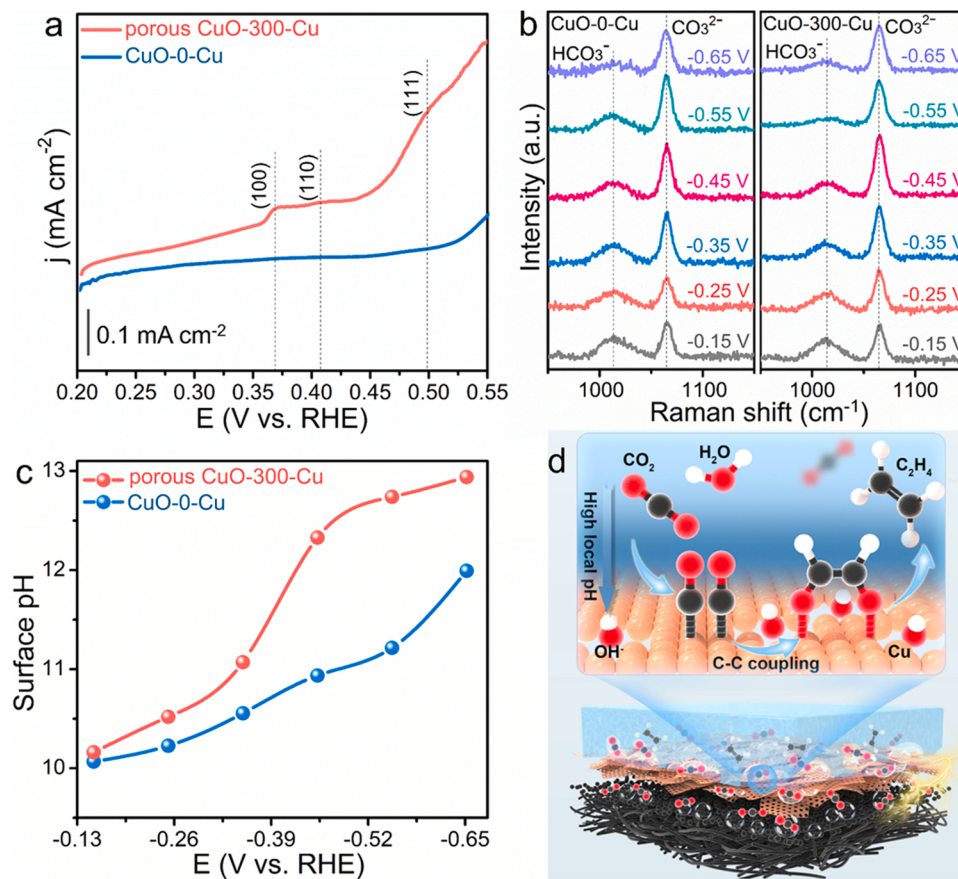


Fig. 2. Analysis of surface microenvironment.
(b) The water contact angles (in the dark green line) and CO₂-contact angles (in the red line) of porous Cu NSs with different nanopore sizes derived from CuO NSs before and after calcination at different temperatures. Schematic illustration of the hydrophilic and hydrophobic properties as well as the accessibility of CO₂ near (b) Cu NSs and (c) porous Cu NSs. Carbon fibers and carbon particles (black), CO₂ bubbles (transparent color), Cu NSs (brownish red), and the electrolyte (light blue).



electrolyte near the electrode. To quantify the relationship between the relative ratio of $[\text{HCO}_3^-]$ to $[\text{CO}_3^{2-}]$ and the local pH, calibration measurements were performed using in-situ Raman spectroscopy by taking spectra at different bulk pH values, as shown in Fig. S11. The integrated Raman peak area ratios for HCO_3^- ($\sim 1012 \text{ cm}^{-1}$, associated with the C-OH stretch of HCO_3^-) and CO_3^{2-} ($\sim 1065 \text{ cm}^{-1}$, associated with the C-O stretch of CO_3^{2-}) [32] could be used to calculate the relative ratio of $[\text{HCO}_3^-]$ to $[\text{CO}_3^{2-}]$, which relates to the relative amounts of HCO_3^- and CO_3^{2-} at or near the surface of the electrode [33]. As shown in Fig. 3b, the peaks for CO_3^{2-} became more prominent as the applied potential increased from -0.15 to -0.65 V , while the peaks for HCO_3^- got weaker, suggesting the increased surface pH for electrode with the increase of the applied potential. The calculated results in Fig. 3c suggest that the surface pH values of porous CuO-300-Cu NSs change from 10.16 to 12.94 when the applied potential increases from -0.15 to -0.65 V , and that for CuO-0-Cu NSs is from 10.07 to 11.99. The much higher surface pH value on porous CuO-300-Cu NSs could be ascribed to the nanoporous structure with the ability to attract and aggregate OH^- from the bulk electrolyte to react with introduced CO_2 to form more CO_3^{2-} in the $\text{CO}_2/\text{HCO}_3^-$ and $\text{HCO}_3^-/\text{CO}_3^{2-}$ equilibrium. Theoretical calculation conducted by Xie et al. demonstrates that the energy barrier of the rate-limiting COCO^* hydrogenation step for C_2H_4 could be decreased under the increased local pH level [24]. Combine with our ECO₂RR test results shown in Fig. 1h, the higher local pH on porous CuO-300-Cu NSs indeed promotes C-C coupling for C_2H_4 formation [34].

ECO₂RR performance of porous CuO-300-Cu NSs in different concentrated KOH electrolyte solutions was also investigated to further verify that the higher local pH is able to enhance the ECO₂RR selectivity to C_2H_4 . As shown in Fig. S12a, both FEs and partial current densities for C_2H_4 in a 3 M KOH electrolyte solution are larger than that in a 1 M KOH electrolyte solution, which demonstrates that the higher concentrated OH^- anions on porous CuO-300-Cu NSs can increase the local pH and

Fig. 3. Analysis of reaction microenvironment. (a) Voltammograms of OH_{ads} peaks collected in 0.1 M KOH aqueous solution. In-situ Raman spectra of (b) CuO-0-Cu NSs and porous CuO-300-Cu NSs with 1 M KOH electrolyte flowing over the electrode and 20 sccm CO_2 on the backside of the electrode at the applied potential ranging from -0.15 to -0.65 V . (c) Surface pH values calculated based on the relation Raman peak area ratios of HCO_3^- to CO_3^{2-} in (b). (d) Schematic illustration of the local reaction microenvironment near porous Cu NSs. Carbon fibers and carbon particles (black), CO_2 bubbles (transparent color), Cu NSs (brownish red), and the electrolyte (light blue).

improve the ECO₂RR selectivity to C_2H_4 . Furthermore, Fig. S12b shows FEs and partial current densities for C_2H_4 on CuO-0-Cu NSs and porous CuO-300-Cu NSs in a 1 M KOH electrolyte solution, exhibiting that porous CuO-300-Cu NSs also exhibit better ECO₂RR selectivity to C_2H_4 . The above results demonstrate that constructing nanoporous structures to regulate the reaction microenvironment with higher local pH can effectively improve the C_2H_4 selectivity of ECO₂RR. A schematic illustration of the local reaction microenvironment near porous Cu NSs with abundant triple-phase junctions and higher local pH to enhance the C_2H_4 selectivity of ECO₂RR is shown in Fig. 3d. OH^- anions adsorption and aggregation on nanoporous Cu NSs lead to higher local pH, which helps to suppress the competing HER, further improve charge transfer kinetics, and decrease the energy barrier of the rate-limiting COCO^* hydrogenation step to a remarkable improvement in selectivity toward C_2H_4 production [24,28].

3.3. Practical application assessment

The electrochemically active surface area (ECSA) of CuO-0-Cu and porous CuO-300-Cu NSs was compared to further explore the advantage of porous structures on Cu NSs for improving ECO₂RR activity. The ECSA was analyzed by calculating the double-layer capacitances (CdL) based on the CV curves at different scan rates (Fig. S13) since ECSA is in proportion to CdL. As shown in Fig. 4a, the CdL value of porous CuO-300-Cu NSs is 8.81 mF cm^{-2} , while that of CuO-0-Cu NSs is only 4.75 mF cm^{-2} , implying that the porous structure is useful to enhance ECSA and improve the intrinsic activity of Cu NSs. Moreover, the porous structure and ultrathin thickness of CuO-300-Cu NSs contribute to leading all active sites to be readily accessible to the reactant on a short timescale, which is also beneficial to improving the ECO₂RR performance.

CuO-0-Cu NSs and porous CuO-300-Cu NSs were used as the catalysts

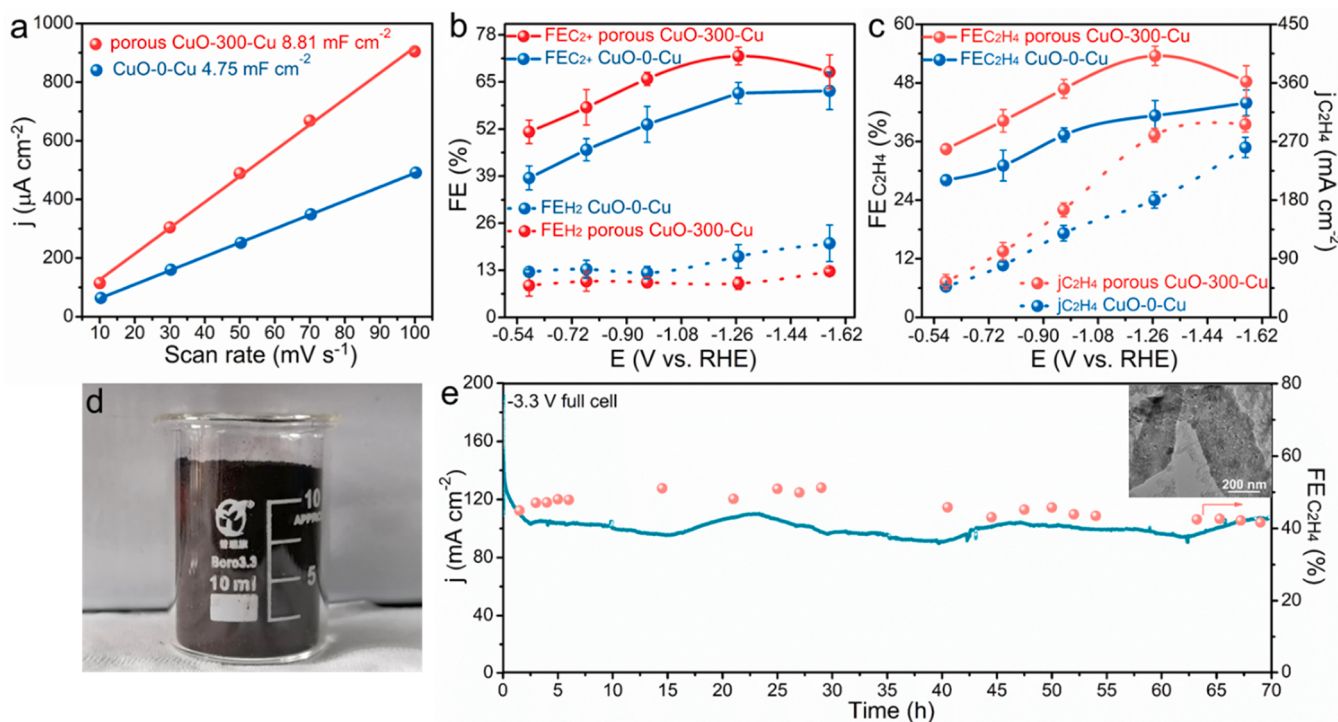


Fig. 4. Practical application assessment. (a) The double-layer capacitances of CuO-0-Cu and porous CuO-300-Cu NSs modified electrodes. (b) FEs for C_2+ products and H_2 on CuO-0-Cu and porous CuO-300-Cu NSs at applied potentials ranging from -0.57 to -1.57 V (without iR correction). (c) FEs and partial current densities for C_2H_4 versus the applied potentials (without iR correction) on CuO-0-Cu and porous CuO-300-Cu NSs. (d) Photograph of the as-prepared porous CuO-300 NSs. (e) The stability of CuO-300-Cu NSs obtained at -3.3 V full cell (without iR correction) in a 2.25 cm^2 MEA electrolyzer using 0.1 M KHCO_3 as the anolyte. Insert image in (e) shows the morphology of porous CuO-300-Cu NSs after ECO₂RR for 70 h.

to compare the ECO₂RR performance at different applied potentials, the product distributions are shown in Fig. S14. Gaseous products including H_2 , CO and C_2H_4 were identified and quantified by gas chromatography spectroscopy (Fig. S15). Liquid products including formic acid, acetic acid, ethanol and isopropanol were identified and quantified by ^1H nuclear magnetic resonance spectroscopy (Fig. S16). According to the test results, the FEs for H_2 on porous CuO-300-Cu NSs are below 15 %, which is lower than that on CuO-0-Cu NS under the whole applied potential range ascribed in Fig. 4b. The FEs for C_2+ products on porous CuO-300-Cu NSs are higher than that on CuO-0-Cu NSs at applied potentials increased from -0.57 to -1.57 V. The maximum FE for C_2+ products on porous CuO-300-Cu NSs reaches $(72.14 \pm 1.45)\%$, which is about 1.2 times larger than that on CuO-0-Cu NSs. Furthermore, as shown in Fig. 4c, the maximum FE for C_2H_4 on porous CuO-300-Cu NSs reaches $(53.54 \pm 1.97)\%$ with a high partial current density for C_2H_4 of $(272.3 \pm 10.5) \text{ mA cm}^{-2}$ at -1.27 V, which is about 1.6 times larger than the partial current density for C_2H_4 on CuO-0-Cu NSs without obvious porous structure. Compared with the current reported Cu-based catalysts, porous CuO-300-Cu NSs also exhibit a certain competitive advantage of high rate conversion of CO_2 to C_2H_4 , as shown in Table S2. Additionally, porous CuO-300 NSs were synthesized by facile precipitation and thermal treatment process with a product yield reaching over 96 %, which is easy to obtain gram-scale production, as shown in Fig. 4d, indicating the potency for practical application. The preliminary stability test of porous CuO-300-Cu NSs was conducted in a membrane electrode assembly (MEA) with a geometric working area of 2.25 cm^2 using 0.1 M KHCO_3 as the anolyte. Fig. 4e shows the stable operation with constant C_2H_4 FE of $(45 \pm 3)\%$ at the applied full-cell voltage of -3.3 V with a current density of $\sim 100 \text{ mA cm}^{-2}$ for about 70 h. Furthermore, the insert image in Fig. 4e and Fig. S17 show the structure and morphology of porous CuO-300-Cu NSs after ECO₂RR for 70 h, which reveals the high structure stable property of in-situ electro-reduced porous Cu NSs during the ECO₂RR process. The exploration of

porous CuO-300-Cu NSs for ECO₂RR in MEA with neutral electrolyte is meaningful for digging into the potency of that for the practical application.

4. Conclusion

Here modulating the surface microstructure of Cu NSs is found to be an effective way to improve the ECO₂RR activity to C_2H_4 . To identify the origin of improved ECO₂RR performance, this work focuses on digging out the inner relationship of microstructure and the induced multiple microenvironments variations on Cu NSs electrodes. Gram-scale production lateral micron-sized Cu NSs with different nanopore sizes were designed as the model catalysts to explore the synergistic effects of microstructure-induced multi-microenvironment variations on ECO₂RR performance. Experimental results show that larger nanopores uniformly distributed on Cu NSs help to modulate the surface microenvironment exhibiting hydrophobic and CO_2 -philic properties, which promote the accessibility of CO_2 to the active sites to facilitate faster CO_2 conversion. ECO₂RR results and in-situ Raman spectra investigation demonstrate that porous structures on Cu NSs also help to adjust the reaction microenvironment maintaining higher local pH near the active sites to further improve the C_2H_4 selectivity of ECO₂RR. In conclusion, constructing porous structures provides a synergistic way for adjusting the surface microstructure and multi-microenvironment to promote the accessibility of CO_2 and the C-C coupling for C_2H_4 formation.

CRediT authorship contribution statement

Dan Wang designed and carried out the experiments, data analysis, and writing-original manuscript. Jia Ning Gui collected the TEM images. Bin Bin Pan directed the MEA experiment. Meng Xuan Li performed the CO_2 -contact angles measurement. Chen Chen Zhang and Jun Jun Mao took part in the in-situ Raman measurement. Yang Lou and Cheng Si Pan

provided resources and guided data analysis. Feng Wang Li, Yu Hang Wang, Yan Guang Li and Yun Kuang took part in the discussion and manuscript review. Yong Fa Zhu contributed to supervising this work and manuscript review. Ying Zhang provided resources, directed research efforts, writing-review & editing the manuscript.

Declaration of Competing Interest

The authors declare that they have no known competing financial interests or personal relationships that could have appeared to influence the work reported in this paper.

Data Availability

Data will be made available on request.

Acknowledgments

This research was supported by the National Natural Science Foundation of China (21902009), Startup Funding at Jiangnan University (1042050205204100, 1045210322190170, 1045281602190010). We also thank the Central Laboratory, School of Chemical and Material Engineering, Jiangnan University.

Appendix A. Supporting information

Supplementary data associated with this article can be found in the online version at [doi:10.1016/j.apcatb.2022.122119](https://doi.org/10.1016/j.apcatb.2022.122119).

References

- [1] D. Gao, R.M. Arán-Ais, H.S. Jeon, B. Roldan Cuenya, Rational catalyst and electrolyte design for CO₂ electroreduction towards multicarbon products, *Nat. Catal.* 2 (2019) 198–210.
- [2] S. Popovic, M. Smiljanic, P. Jovanovic, J. Vavra, R. Buonsanti, N. Hodnik, Stability and degradation mechanisms of copper-based catalysts for electrochemical CO₂ reduction, *Angew. Chem. Int. Ed.* 59 (2020) 14736–14746.
- [3] S. Nitopi, E. Bertheussen, S.B. Scott, X. Liu, A.K. Engstfeld, S. Horch, B. Seger, I.E. L. Stephens, K. Chan, C. Hahn, J.K. Norskov, T.F. Jaramillo, I. Chorkendorff, Progress and perspectives of electrochemical CO₂ reduction on copper in aqueous electrolyte, *Chem. Rev.* 119 (2019) 7610–7672.
- [4] J.J. Wang, X.P. Li, B.F. Cui, Z. Zhang, X.F. Hu, J. Ding, Y.D. Deng, X.P. Han, W. B. Hu, A review of non-noble metal-based electrocatalysts for CO₂ electroreduction, *Rare Met.* 40 (2021) 3019–3037.
- [5] S.L. Chu, X. Li, A.W. Robertson, Z.Y. Sun, Electrocatalytic CO₂ reduction to ethylene over CeO₂-supported Cu nanoparticles: effect of exposed facets of CeO₂, *Acta Phys. -Chim. Sin.* 37 (2021), 2006034.
- [6] W. Ye, X. Guo, T. Ma, A review on electrochemical synthesized copper-based catalysts for electrochemical reduction of CO₂ to C₂₊ products, *Chem. Eng. J.* 414 (2021), 128825.
- [7] M. Ebaid, K. Jiang, Z. Zhang, W.S. Drisdell, A.T. Bell, J.K. Cooper, Production of C₂/C₃ oxygenates from planar copper nitride-derived mesoporous copper via electrochemical reduction of CO₂, *Chem. Mater.* 32 (2020) 3304–3311.
- [8] G.L. De Gregorio, T. Burdyny, A. Loiudice, P. Iyengar, W.A. Smith, R. Buonsanti, Facet-dependent selectivity of Cu catalysts in electrochemical CO₂ reduction at commercially viable current densities, *ACS Catal.* 10 (2020) 4854–4862.
- [9] M. Li, Y. Ma, J. Chen, R. Lawrence, W. Luo, M. Sacchi, W. Jiang, J. Yang, Residual chlorine induced cationic active species on a porous copper electrocatalyst for highly stable electrochemical CO₂ reduction to C₂₊, *Angew. Chem. Int. Ed.* 60 (2021) 11487–11493.
- [10] A. Loiudice, P. Lobaccaro, E.A. Kamali, T. Thao, B.H. Huang, J.W. Ager, R. Buonsanti, Tailoring copper nanocrystals towards C₂ products in electrochemical CO₂ reduction, *Angew. Chem. Int. Ed.* 55 (2016) 5789–5792.
- [11] H.Z. Yang, L. Shang, Q.H. Zhang, R. Shi, G.I.N. Waterhouse, L. Gu, T.R. Zhang, A universal ligand mediated method for large scale synthesis of transition metal single atom catalysts, *Nat. Commun.* 10 (2019) 1–9.
- [12] Z. Chen, T. Wang, B. Liu, D. Cheng, C. Hu, G. Zhang, W. Zhu, H. Wang, Z.J. Zhao, J. Gong, Grain-boundary-rich copper for efficient solar-driven electrochemical CO₂ reduction to ethylene and ethanol, *J. Am. Chem. Soc.* 142 (2020) 6878–6883.
- [13] J. Wang, C. Cheng, B. Huang, J. Cao, L. Li, Q. Shao, L. Zhang, X. Huang, Grain-boundary-engineered La₂CuO₄ perovskite nanobamboos for efficient CO₂ reduction reaction, *Nano Lett.* 21 (2021) 980–987.
- [14] B. Zhang, J. Zhang, M. Hua, Q. Wan, Z. Su, X. Tan, L. Liu, F. Zhang, G. Chen, D. Tan, X. Cheng, B. Han, L. Zheng, G. Mo, Highly electrocatalytic ethylene production from CO₂ on nanodefective Cu nanosheets, *J. Am. Chem. Soc.* 142 (2020) 13606–13613.
- [15] F. Scholten, K.C. Nguyen, J.P. Bruce, M. Heyde, B. Roldan Cuenya, Identifying structure-selectivity correlations in the electrochemical reduction of CO₂: a comparison of well-ordered atomically clean and chemically etched copper single-crystal surfaces, *Angew. Chem. Int. Ed.* 60 (2021) 19169–19175.
- [16] G. Li, T. Yan, X. Chen, H. Liu, S. Zhang, X. Ma, Electrode engineering for electrochemical CO₂ reduction, *Energy Fuels* 36 (2022) 4234–4249.
- [17] R. Shi, J.H. Guo, X.R. Zhang, G.I.N. Waterhouse, Z.J. Han, Y.X. Zhao, L. Shang, C. Zhou, L. Jiang, T.R. Zhang, Efficient wettability-controlled electroreduction of CO₂ to CO at Au/C interfaces, *Nat. Commun.* 11 (2020) 1–10.
- [18] P. An, L. Wei, H. Li, B. Yang, K. Liu, J. Fu, H. Li, H. Liu, J. Hu, Y.-R. Lu, H. Pan, T.-S. Chan, N. Zhang, M. Liu, Enhancing CO₂ reduction by suppressing hydrogen evolution with polytetrafluoroethylene protected copper nanoneedles, *J. Mater. Chem. A* 8 (2020) 15936–15941.
- [19] Y. Zhang, Z. Cai, Y. Zhao, X. Wen, W. Xu, Y. Zhong, L. Bai, W. Liu, Y. Zhang, Y. Zhang, Y. Kuang, X. Sun, Superaerophilic copper nanowires for efficient and switchable CO₂ electroreduction, *Nanoscale Horiz.* 4 (2019) 490–494.
- [20] Z.L. Yu, S.Q. Wu, L.W. Chen, Y.C. Hao, X. Su, Z. Zhu, W.Y. Gao, B. Wang, A.X. Yin, Promoting the electrocatalytic reduction of CO₂ on ultrathin porous bismuth nanosheets with tunable surface-active sites and local pH environments, *ACS Appl. Mater. Interfaces* 14 (2022) 10648–10655.
- [21] W. Luo, J. Zhang, M. Li, A. Züttel, Boosting CO production in electrocatalytic CO₂ reduction on highly porous Zn catalysts, *ACS Catal.* 9 (2019) 3783–3791.
- [22] C.T. Dinh, T. Burdyny, M.G. Kibria, A. Seifitokaldani, C.M. Gabardo, F.P. García de Arquer, E.H. Sargent, CO₂ electroreduction to ethylene via hydroxide-mediated copper catalysis at an abrupt interface, *Science* 360 (2018) 783–787.
- [23] Y. Wang, Z. Wang, C.-T. Dinh, J. Li, A. Ozden, M. Golam Kibria, A. Seifitokaldani, C.-S. Tan, C.M. Gabardo, M. Luo, H. Zhou, F. Li, Y. Lum, C. McCallum, Y. Xu, M. Liu, A. Proppe, A. Johnston, P. Todorovic, T.-T. Zhuang, D. Sinton, S.O. Kelley, E.H. Sargent, Catalyst synthesis under CO₂ electroreduction favours faceting and promotes renewable fuels electrosynthesis, *Nat. Catal.* 3 (2019) 98–106.
- [24] Y. Zhao, X. Zu, R. Chen, X. Li, Y. Jiang, Z. Wang, S. Wang, Y. Wu, Y. Sun, Y. Xie, Industrial-current-density CO₂-to-C₂₊ electroreduction by anti-swelling anion-exchange ionomer-modified oxide-derived Cu nanosheets, *J. Am. Chem. Soc.* 144 (2022) 10446–10454.
- [25] J. Qiao, Y. Liu, F. Hong, J. Zhang, A review of catalysts for the electroreduction of carbon dioxide to produce low-carbon fuels, *Chem. Soc. Rev.* 43 (2014) 631–675.
- [26] P.O. Larsson, A. Andersson, Complete oxidation of CO, ethanol, and ethyl acetate over copper oxide supported on titania and ceria modified titania, *J. Catal.* 179 (1998) 72–89.
- [27] L. Debichi, M.C. Marco de Lucas, J.F. Pierson, P. Krüger, Vibrational properties of CuO and Cu₄O₃ from first-principles calculations, and Raman and infrared spectroscopy, *J. Phys. Chem. C* 116 (2012) 10232–10237.
- [28] G. Wang, J. Chen, Y. Ding, P. Cai, L. Yi, Y. Li, C. Tu, Y. Hou, Z. Wen, L. Dai, Electrocatalysis for CO₂ conversion: from fundamentals to value-added products, *Chem. Soc. Rev.* 50 (2021) 4993–5061.
- [29] J.J. Lv, R. Yin, L. Zhou, J. Li, R. Kikas, T. Xu, Z.J. Wang, H. Jin, X. Wang, S. Wang, Microenvironment engineering for the electrocatalytic CO₂ reduction reaction, *Angew. Chem. Int. Ed.* (2022), e202207252.
- [30] D. Raciti, L. Cao, K.J.T. Livi, P.F. Rottmann, X. Tang, C. Li, Z. Hicks, K.H. Bowen, K. J. Hemker, T. Mueller, C. Wang, Low-overpotential electroreduction of carbon monoxide using copper nanowires, *ACS Catal.* 7 (2017) 4467–4472.
- [31] C. Choi, S. Kwon, T. Cheng, M. Xu, P. Tieu, C. Lee, J. Cai, H.M. Lee, X. Pan, X. Duan, W.A. Goddard, Y. Huang, Highly active and stable stepped Cu surface for enhanced electrochemical CO₂ reduction to C₂H₄, *Nat. Catal.* 3 (2020) 804–812.
- [32] K.A. Willets, R.P. Van Duyne, Annu. Localized surface plasmon resonance spectroscopy and sensing, *Rev. Phys. Chem.* 58 (2007) 267–297.
- [33] A.R. Davis, B.G. Oliver, A vibrational-spectroscopic study of the species present in the CO₂-H₂O system, *J. Solut. Chem.* 1 (1972) 329–339.
- [34] G. Iijima, T. Inomata, H. Yamaguchi, M. Ito, H. Masuda, Role of a hydroxide layer on Cu electrodes in electrochemical CO₂ reduction, *ACS Catal.* 9 (2019) 6305–6319.